Geopersia 2024, 14(1): 213-229
DOI: 10.22059/GEOPE.2024.360437.648717

RESEARCH PAPER

Geochemical prospectivity of Au mineralization through Concentration-Number fractal modelling and Prediction-Area plot: a case study in the east of Iran

Ashkan Seydi, Maysam Abedi *, Abbas Bahroudi, Hosein Ferdowsi

School of Mining Engineering, College of Engineering, University of Tehran, Tehran, Iran

Received: 06 June 2023, Revised: 22 January 2024, Accepted: 12 February 2024

Abstract
Birjand region is located in South Khorasan province in the structural-magmatic zone of eastern Iran. This part of the Iranian plateau is the result of subduction during the Cenozoic and subsequent continental collisions. This region is known as important in terms of copper and gold mineralization for various geological reasons. This research aims to develop a map of Au geochemical potential. 1966 geochemical samples were collected in the study area, and a 20-element analysis was performed. After data pre-processing including correction of outlier data and data normalization, and through a graph from the fractal concentration-number (C-N) model to isolate different geochemical populations of Au, As, Sb, Hg, Bi, Mo, Sn, and W with Au targeting, a Prediction-area (P-A) graph was plotted for each variable to determine the weight of each geochemical indicator. The results show that after gold, with an ore prediction rate of 74% and specifying 26% of the studied district as mineralization-prone areas, arsenic with a prediction rate of 72% has covered 28% of the Birjand region as potential mineralization areas while Bismuth and Mercury with a prediction of 64% covered 36% of the Birjand region. In addition, a hybrid indicator map was prepared utilizing a multi-class index overlay method, where the potential geochemical areas were located further south and southeast of Birjand. In addition, there are favourable areas in the middle. Notably, the mineral potential map (MPM) has higher efficiency than any geochemical indicator, with an ore prediction rate of 88% and occupying 12% of the whole prospect area.

Keywords: Concentration-Number Fractal (C-N), Prediction-Area Plot (P-A), MPM, Au, Birjand.

Introduction

Cu (–Mo– Au) porphyry deposits are the world's primary source of Copper and Molybdenum and an essential source of gold. The sheer volume of these reserves makes them attractive exploration targets. Most porphyry copper deposits worldwide are associated with subduction-related calc-alkaline magmas and occur spatially in magmatic arcs (Mitchell, 1973; Sillitoe, 1972; Camus et al., 1996; Cooke et al., 2005). Classical regions in the continental arc configuration in the central Andean are considered oceanic subduction plate flattening, crustal thickening, and associated block elevation (Skewes & Stern, 1995; Kay et al., 1999; Richards et al., 2001; Bissig et al., 2003; Perello et al., 2003; Cooke et al., 2005). Porphyry sediments occur in the structure of island arcs throughout the western Pacific and are mainly controlled by faults along with the parallel arc faults, and transverse arc faults are related to the rupture of subducted slabs (Sillitoe, 1993; Kerrich et al., 2000; Corbett & Leach, 1998). These sediments

* Corresponding author e-mail: MaysamAbedi@ut.ac.ir

are formed from hydrothermal fluids released from hydrogen arc magmas with high sulfur. The mentioned sediments are from a metasomatized wedge mantle obtained by subducted slab fluids (Peacock, 1993; Arculus, 1994). Classical sections for such deposits are found in the Himalayan-Tibetan orogeny in the metallogenic belt of Eastern Tethyan. Giant Copper-Molybdenum and Copper-Gold porphyry deposits exist in both the southern and eastern parts of Tibet (such as the Yulong and Gangdese porphyry copper belts). Studies to find porphyry deposits in the Birjand region need to be widely developed. Still, due to the geological structures of the Birjand region and its location, which is almost on the porphyry mineralization belt of Iran, starting from the northwest to the southeast, the possibility of porphyry deposits in this area is very high.

Separating the geochemical anomalies is a helpful tool for geochemical exploration. Anomalous thresholds, the most beneficial criterion for cross-checking information with numerical data from different sources, are commonly used in geochemical studies (Hou et al., 2011; Harris et al., 1999; Cheng, 1999; Cheng et al., 1996). Mineral capacity forecasting modelling using the Geographic Information System (GIS) is a valid and accepted tool for drawing reproducible mineral exploration goals. Abnormal geochemical areas can be defined by more than a particular threshold value. Different statistical methods based on a specific assumption about the statistical distribution of geochemical variables to determine the values of anomaly threshold, for the separation of geochemical provinces concerning the mineral deposit's purpose, have attracted scientists' attention (Ghavami-Riabi et al., 2010; Darabi-Golestan et al., 2013; Seyedrahimi-Niaraq & Hekmatnejad, 2020). Recognition and separating anomalous areas from the background are an integral part of any geochemical exploration research (Qiuming, 2000; Hawkes & Webb, 1979).

Different versions of fractal/multi-fractal modelling, developed by Mandelbrot (1983), have been proposed to analyze geochemical data. Numerous studies have been devoted to the use of these versions: number-size (N-S) by Mandelbrot (1983), concentration-area (C-A) by Cheng et al. (1994), distance-concentration (C-D) by Li et al. (2003), concentration-volume (C-V) by Afzal et al. (2011, 2013) and concentration- number (C-N) by Hassanpour & Afzal (2013). One of the main features of fractal models compared to statistical methods is considering the spatial status of informational samples (Zuo, 2011; Ghaeminejad et al., 2020), which reflects a region's geological, geochemical, and mineralogical sequences. Based on fractal analysis (Zuo & Wang, 2016; Panahi et al., 2004; Mohammadpour et al., 2019), it can deduce geochemical indicators to prepare the mineral potential map (MPM).

In MPM, the location of known deposits can be used to evaluate forecasting models' performance, which is achieved by covering mineral deposit sites on an exploratory classified model (Mirzaie et al., 2020; Nykanen et al., 2015; Yousefi & Carranza, 2015). MPM is a multi-criterion decision-making (MCDM) function that aims to map and prioritize suitable areas to identify undiscovered mineral reserves of the desired type (Carranza & Laborte, 2016). Bonham-Carter et al. (1989) used the weight of spatial index classes divided by their respective area covered (area occupied by each type of proven values) to estimate the probability of discovering mineral deposits in several classes, primarily by fractal analysis. Yousefi & Carranza (2015, 2016) developed the Prediction-Area plot (P-A), through which the percentage of known deposits predicted by the forecasting layers (forecast rate) and the desired areas of the respective forecasting classes help to determine the comparative importance of different forecasting models. By plotting the P-A diagram, the deposit rate and the desired region for the exploration targets' mineralization help the forecast models (Du et al., 2016; Gao et al., 2016; Nezhad et al., 2017; Zhang et al., 2017; Almasi et al., 2017). Therefore, if two forecasting models plot exploratory targets with other desired regions but with the exact prediction value, the model's performance with smaller target areas is higher than that with larger target areas (Roshanravan et al., 2019).

The primary purpose of this study is to identify geochemical anomalies in the Mokhtaran, Basiran, Dehsalm, and Kardegan areas under a single map using stream sediment samples. Through multivariate analysis of geochemical clustering data and principal component analysis (PCA), several indicators are prepared to be displayed at intervals indicating the usefulness of Au after pre-processing all input elements. This area is a polymetallic region where, in addition to gold mineralization, there is also copper, lead and zinc mineralization in it (Seydi et al., 2023). Simultaneous consideration of the C-N fractal curve and the P-A diagram provides information about the data-driven weights of each indicator map. At the end of the process, a data-driven multi-class index overlay method is developed to predict Au occurrence more accurately.

Geology of the study area

The structural zoning map of Iran (Figure 1) was prepared by Agha-Nabati in 2005, in which the study area is specified. The map of the study area (Figure 2) includes four maps of Basiran (the right one in the middle third), Kardegan (the left one in the middle third), the Mokhtaran (in the upper third), and the Dehsalm (in the lower third), that each of them was prepared in a 1: 100,000 scale by the Geological Survey of Iran. Due to differences in the map legend as well as minimal differences at the intersection in the corresponding points at the exact coordinates, it is prepared in an integrated manner.

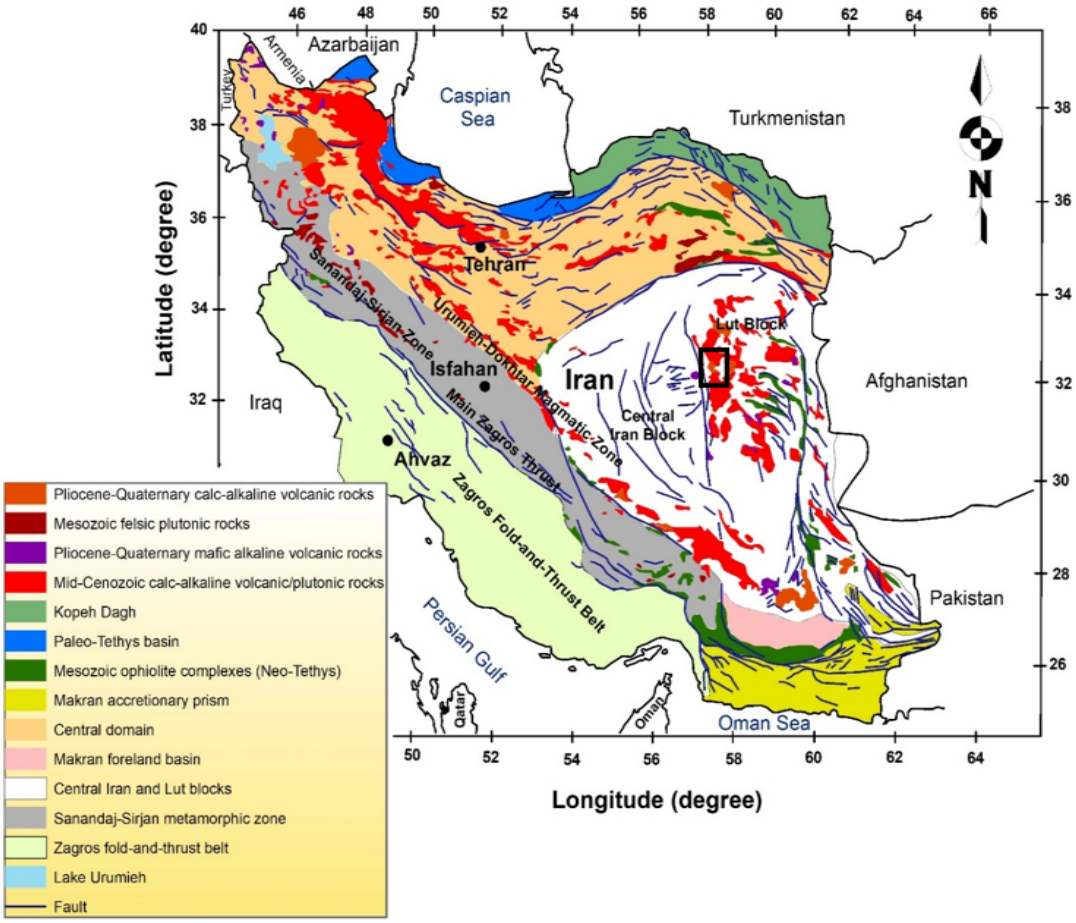

Figure 1. Structural geological map of Iran on which the location of the study area is specified (prepared by Aghanabati, 2005 and Richards et al, 2006; reproduced by Abedi et al., 2018)

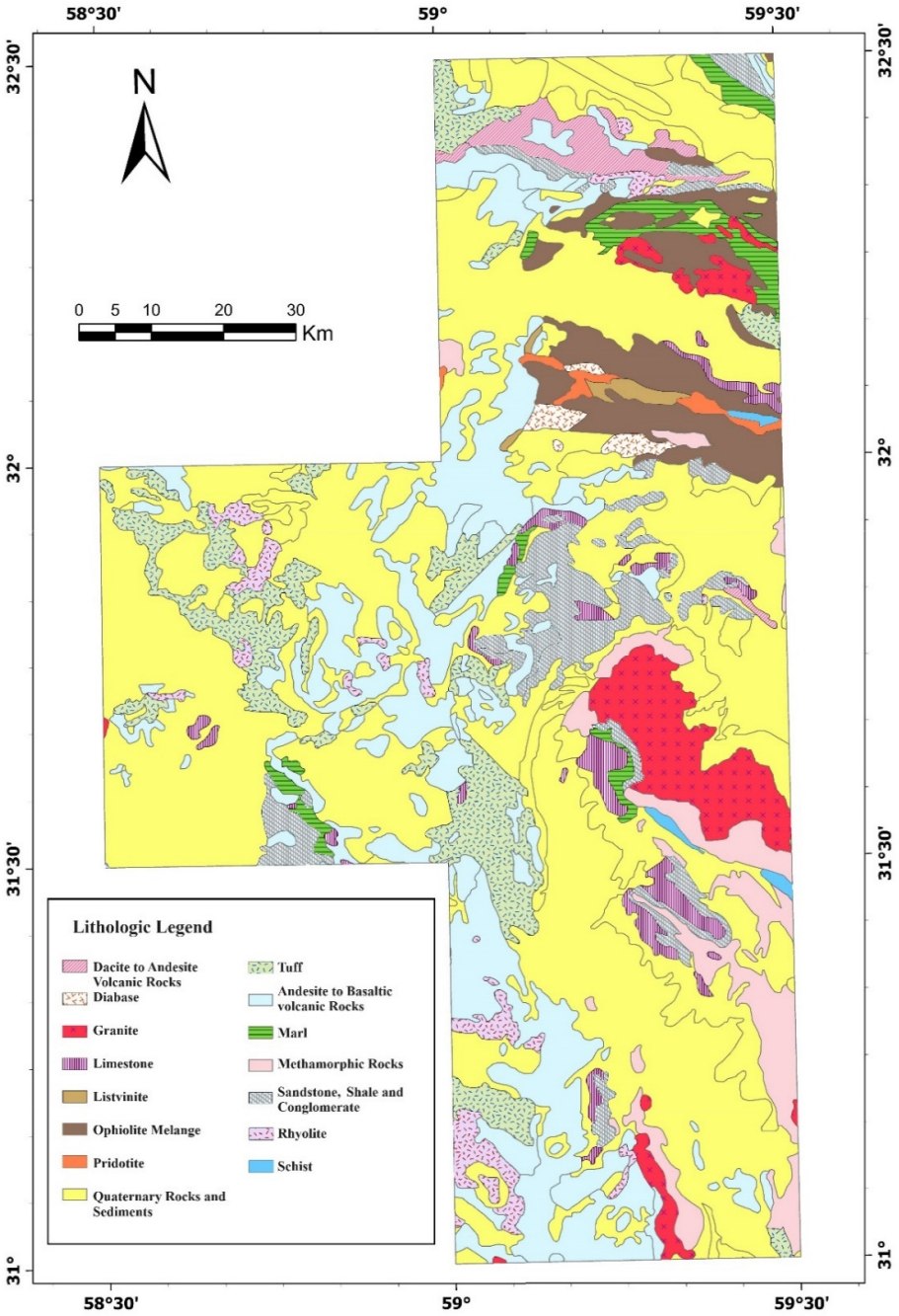

Figure 2. The detailed geological map with 1: 100,000 scale. The study area consists of the regions of Basiran, Dehsalm, Kardegan, and Mokhtaran

The unique geological and tectonic position of the Mokhtaran region, located in the southern part of Birjand city, located in South Khorasan province, has made this region a good potential for the occurrence of porphyry copper and epithermal gold ores. The presence of young intrusive masses in the region, such as microgranodiorite, and the presence of Paleogene volcanic as hosts are essential indicators of epithermal gold and porphyry copper mineralization in the area. Significant alterations that represent porphyry copper and epithermal gold minerals in this region include propylitic alteration (calcite, epidote, and chlorite minerals), argillic and sericite alteration (malachite and azurite minerals, which are part of the hydroxyl minerals group) and iron oxides alteration (goethite, hematite, and lepidocrocite).

In the Basiran region, due to its unique geological conditions and many magmatic activities in different geological eras, it is possible to find different types of mineralization such as epithermal, porphyry, and veins; for example, we can mention the Qale-Zari copper-gold mine. This region's eastern and central part is mainly covered by Mesozoic and Tertiary sediments and volcanic rocks. The rock units of the Basiran region can be divided into five groups: sedimentary rocks, plutonic and hypabyssal igneous rocks, lavas, pyroclastic rocks, and skarns. The oldest stratigraphic unit in the study area is Jurassic shale and sandstone. Paleocene base conglomerates are brown and massive, and thick cream-coloured limestone containing Paleocene microfossils are metamorphosed on lava, sandstone lavas and pyroclastic rocks belonging to the Eocene which are cut off by the plutonic and hypabyssal rocks. In some parts of this area, Neogene conglomerates up to 50 m thickness are located on Eocene lavas and tuffs. Massifs such as granodiorite, granite, and diorite are exposed in different parts of this region, attributed to the Mesozoic and Tertiary geological periods (Seydi et al., 2023).

Dehsalm region is mainly covered by volcanic rocks of the third era with a significant andesitic-dacite composition, so the various parts are covered by sand and volcanic rocks with a dark appearance. The rocks of this region can be divided into internal and external. The inner rocks include granophyre, quartzite, and syenite, and green diorite is seen in the heights of the region. The external rocks of this area include basaltic andesite with a greyish-green colour and dacite with a cream-to-pink colour; all the site's outer rocks have been affected by argillic, propylitic, and siliceous alterations. Metabasite rocks are well spread in the Dehsalm area and can combine amphibolite, meta-basalts, basalts, calc silicates, schists, and occlusions.

In the Kardegan region, intense and continuous volcanic activity in the Middle Jurassic can be named the most important geological activity, along with landslide faults and gentle folds. Shale, sandstone, and Lower Jurassic to Upper Cretaceous limestones can be found in the old layers of this area, which have been severely wrinkled in some areas. Some of the rocks in the Kardegan area have been transformed into slate and schist. Plutonic and hypabyssal igneous rock of this region include from Eocene to Oligocene and as one of the igneous units, dark basaltic lavas are the most widespread in the area. Among the igneous rock, we can point to the almost acidic rocks of dacite and rhyolite with porphyry texture and basalt to acidic tuffs, all three of which are part of hypabyssal igneous rock. The only plutonic igneous units are diorite and granodiorite, which due to being covered by Quaternary alluvium, only small protrusions can be seen in the region.

Birjand region, due to subduction, a significant volume of magmatism activities in the form of volcanic events and the placement of intrusive masses in this region has been done. There are intrusive masses of granodiorite, quartz diorite, and diorite with Eocene age, as reported in the Urmia-Dokhtar belt. In addition to these intrusive bunches, volcanic rocks like basalt, andesitic basalt, andesite and their associated pyroclastic have been reported. Some igneous rocks are in the form of stocks within volcanic units in the region. Pyroclastic and volcanic deposits are commonly seen on and around stocks. Geochemical and petrological evidence suggests these igneous massifs formed in a subduction zone. There is evidence of magmatic mixing between the submerged lithosphere and crustal rocks. The intrusive masses are generally located petrologically in the calc-alkaline to Shoshonitic series and characterize the continental arc environment with enriched mantle origin and subduction-zone fluids' effect.

As a result of magmatic activity and subsequent events, various minerals such as copper, molybdenum, gold, and silver have been formed. Some of these minerals are in veins form, massive sulfides, and skarn deposits, while others have been reported as porphyries. In the study area, according to the studies that have been done and the comprehensive map prepared by the Geological Survey and Mineral Exploration of Iran regarding the distribution of mines in the country, there are active mines in the Mokhtaran region that have copper mineralization and other minerals. Khonik mine is a low-sulfide epithermal mine whose mineralization is gold,

silver, copper, and boron located in the geological unit of volcanic and agglomerated sections of the Eocene period. The Copper-Gold mine of Chah-Zaghoo is a porphyry-skarn type, and its host rock is granite. In the Kardegan area, a porphyry Copper mine well-known as Chah-Shalghami is located in the andesite-basalt and grey to black basalts. The Qale-Zari mine, situated in andesitic lavas, semi-deep equations, and tuff, is an IOCG ore deposit whose main ores are copper and gold (Sillitoe, 2003).

Research method

Analysis of geochemical data

Table 1 contains statistical properties such as the number of samples in the region for each studied element and their maximum, minimum, mean, and standard deviation, including As, Au, Bi, Hg, Mo, Sb, Sn and W. The histograms of geochemical concentration distribution are shown in the first and third columns of Figure 3. Their box diagrams are shown in the second and fourth columns of Figure 3, which eliminate outlier data for a better geochemical potential map. Simultaneously examining the histogram of geochemical concentration distribution and box diagrams, general information about how the data is distributed in terms of concentration is obtained.

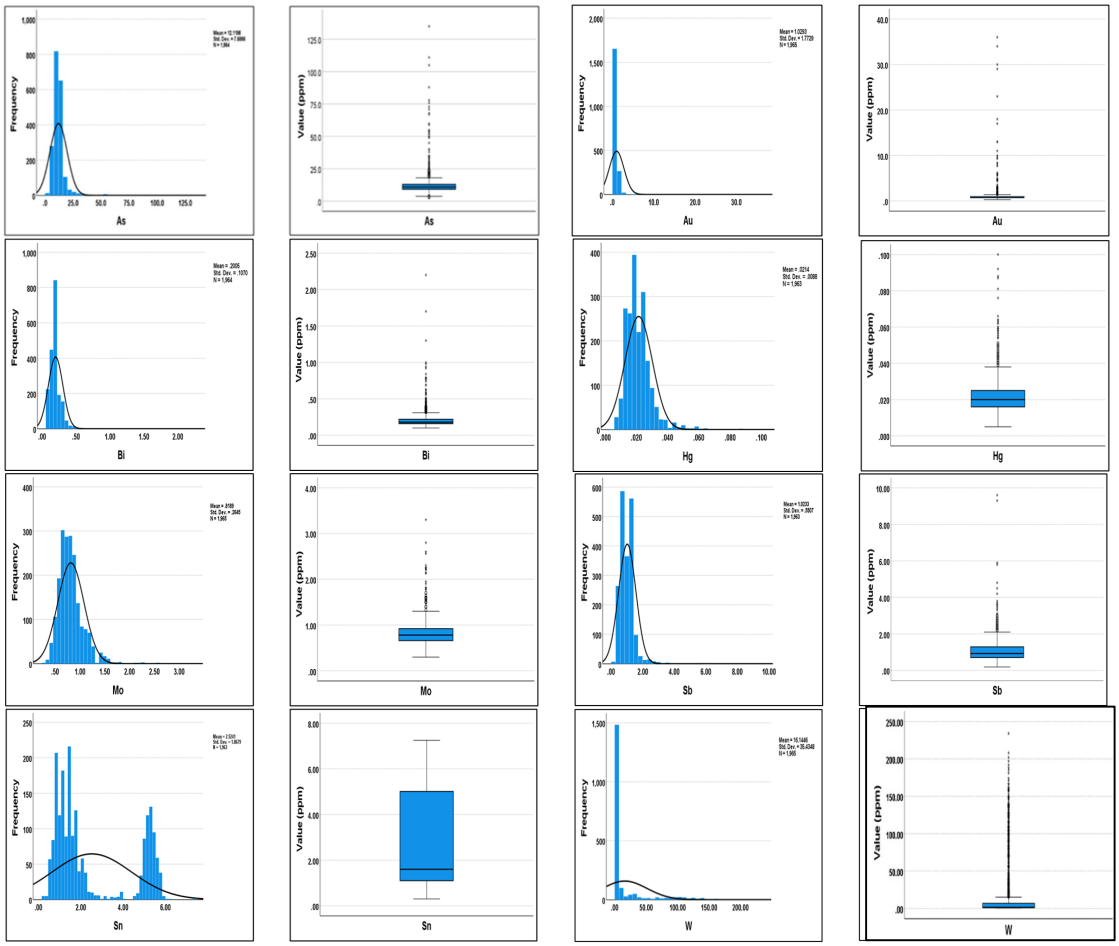

Figure 3. Statistical graphs consist of a geochemical concentration distribution histogram (left column) and box diagram (right column) for Arsenic and Gold (row 1), Bismuth and Mercury (row 2), Molybdenum and Antimony (row 3), Tin and Tungsten (row 4) respectively

Table 1. Statistical characteristics of the most important paragenesis related to gold mineralization

	Number	Minimum	Maximum	Mean	Standard Deviation
As	1964	3.1000	135.0000	12.1198	7.6885
Au	1965	0.3000	36.0000	1.0293	1.7729
Bi	1964	0.1000	2.2000	0.2005	0.1070
Hg	1963	0.0050	0.1000	0.0214	0.0088
Mo	1965	0.3000	3.3000	0.8189	0.2645
Sb	1963	0.1900	9.6000	1.0233	0.5507
Sn	1963	0.3000	7.2510	2.5241	1.8679
W	1965	0.5000	234.0000	16.1446	35.4348

One of the methods that can be widely used in studying geochemical models is multivariate statistical methods that allow the classification and ranking of geochemical anomalies (Tahernejad et al., 2018). For example, we can mention the correlation of the coefficient method between the elements, which can determine the relationship between the elements and the main variables related to the case study mineralization. The correlation between the elements can also be investigated using the clustering method (Riemann et al., 2002; Nazarpour et al., 2015), in which the correlation between 17 geochemical variables is shown in the dendrogram of Figure 4. The following section determines the relationship between the gold element and 16 other chemical variables using the Pearson method, as shown in Table 2. In the dendrogram, most of the gold correlation is with bismuth, arsenic, molybdenum, mercury and antimony. In contrast, by using the values obtained from the Pearson correlation coefficient, it has the highest correlation with strontium at 0.299 and then with mercury at 0.186.

Factor analysis is a dimensional tool in statistical analysis (Khalifani et al., 2019; Grant, 1990; Zumlot, 2012), which has attracted the attention of researchers to find the main factor among several geochemical variables. Multivariate statistical analysis, especially factor analysis, is suitable for behavioural characteristics and reducing the number of geochemical variables. It has been widely used in factor analysis to interpret geochemical data of stream sediments. The ultimate goal of factor analysis is to explain the types of multivariate data by as many factors as possible and to identify the hidden multivariate data structure. Factor analysis is suitable for interpreting the inherent variability in a geochemical data set with many input elements being analyzed. As a result, factor analysis is often a powerful tool for analyzing exploratory data (Li et al., 2003).

Principal component analysis was performed for the geochemical data of the stream sediments to reduce the variables, where Table 3 lists eight elements and three main factors. The elements selected for factor analysis are based on the previous two methods and paragenesis associated with gold in most deposits. The main variables of each factor are determined based on the values obtained in each of the factors, which in the first factor are: tin, tungsten, and bismuth; in the second factor are arsenic and antimony; and in the third factors are mercury, gold and molybdenum.

Concentration-Number fractal analysis

Fractal methods show the relationship between geological, geochemical, and mineralogical information (Panahi et al., 2004). Among several versions of fractal methods, the concentration-number (C-N) model can be used to explain how the geochemical population is distributed without pre-analyzing the data (Karar et al., 2006; Sprovieri et al., 2020). This model shows a spatial relationship between the input property and the sample values. The following equation can define the C-N model:

$$N(>\rho) = F\rho^{-D} \quad (1)$$

Where ρ is the concentration of the element and $N(>\rho)$ is the total number of samples whose concentration is equal to or greater than ρ, F is also a constant, and D is a standard power for

the fractal dimensions of the concentration distribution. In addition, an N ($> \rho$) versus ρ curve in a log diagram represents linear segments with different -D slopes corresponding to different concentration ranges (Sprovieriv et al., 2020; Nabatian et al., 2015; Hirst, 1974; Malinowski & Howery, 1980; Wu et al., 2020).

As can be seen from the C-N logarithmic diagram for the Gold (Au) variable, according to Figure 5-a, there are four geochemical populations, which, considering the importance of this variable and the low value for gold in the Clark table in general, have three populations as anomalous values with the threshold of 0.11, shown in Figure 5-c in yellow and orange, and contains values above 4 ppm.

Based on the C-N logarithmic diagram, the five geochemical populations for Arsenic (As) are shown in Figure 6-a, and it can be said that the anomalous area's threshold is equal to 0.58 and shows grade values that are greater than 78.3 ppm, which are shown in Figure 6-c.

For the Antimony (Sb) variable in the C-N logarithmic diagram, five geochemical populations are considered; by considering the population trends and also the difference between them in Figure 7-A, only the last population is regarded as an anomalous population and has a value of 0.69 and is also shown in Figure 7-C as a C-N logarithmic diagram in red and applies to carats greater than 6.624 ppm.

Table 2. Pearson correlation of coefficient of the most important elements

Zn	**1.000**																
Pb	**0.610**	**1.000**															
Ag	**0.630**	**0.867**	**1.000**														
Cr	**0.351**	**0.483**	**0.576**	**1.000**													
Ni	**0.413**	**0.615**	**0.649**	**0.639**	**1.000**												
Bi	**0.415**	**0.351**	**0.376**	**0.500**	**0.227**	**1.000**											
Cu	**0.392**	**0.717**	**0.751**	**0.401**	**0.627**	**0.054**	**1.000**										
As	**0.333**	**0.449**	**0.454**	**0.625**	**0.268**	**0.582**	**0.122**	**1.000**									
Sb	**0.463**	**0.604**	**0.661**	**0.655**	**0.359**	**0.504**	**0.420**	**0.694**	**1.000**								
Co	**0.637**	**0.694**	**0.766**	**0.542**	**0.745**	**0.384**	**0.612**	**0.323**	**0.503**	**1.000**							
Sn	**0.573**	**0.802**	**0.902**	**0.634**	**0.682**	**0.417**	**0.683**	**0.507**	**0.615**	**0.776**	**1.000**						
Ba	**0.429**	**0.676**	**0.741**	**0.476**	**0.297**	**0.489**	**0.509**	**0.507**	**0.666**	**0.509**	**0.657**	**1.000**					
Sr	**0.452**	**0.165**	**0.165**	**0.317**	**0.085**	**0.584**	**-0.102**	**0.399**	**0.342**	**0.272**	**0.118**	**0.427**	**1.000**				
Hg	**0.236**	**-0.352**	**-0.405**	**-0.334**	**-0.274**	**0.032**	**-0.320**	**-0.174**	**-0.223**	**-0.076**	**-0.434**	**-0.299**	**0.381**	**1.000**			
W	**0.230**	**0.295**	**0.219**	**0.058**	**-0.028**	**0.052**	**0.175**	**0.160**	**0.207**	**0.071**	**0.286**	**0.211**	**-0.274**	**-0.018**	**1.000**		
Mo	**0.309**	**0.626**	**0.648**	**0.233**	**0.392**	**-0.029**	**0.530**	**0.087**	**0.249**	**0.436**	**0.689**	**0.263**	**-0.504**	**-0.260**	**0.209**	**1.000**	
Au	**0.087**	**-0.096**	**-0.152**	**-0.076**	**-0.050**	**0.060**	**-0.068**	**0.051**	**0.001**	**-0.093**	**-0.235**	**-0.073**	**0.299**	**0.186**	**-0.060**	**-0.171**	**1.000**
	Zn	Pb	Ag	Cr	Ni	Bi	Cu	As	Sb	Co	Sn	Ba	Sr	Hg	W	Mo	Au

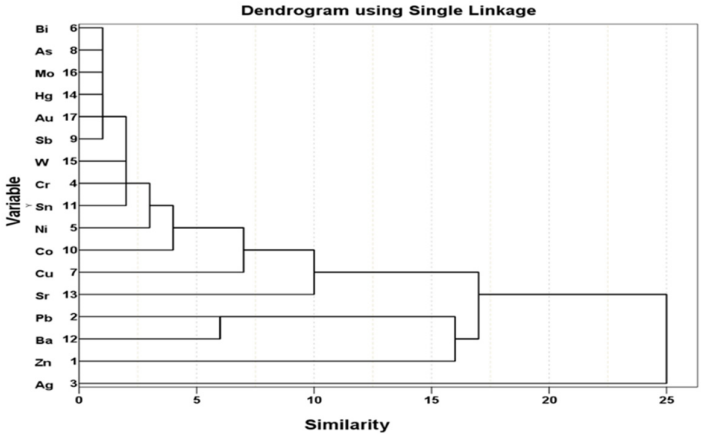

Figure 4. Dendrogram analysis of element concentrations in the study area

Table 3. Principal Component Analysis (PCA) of the most important elements and display of components

	C1	C2	C3
Sn	**-0.727**	0.395	0.129
W	**-0.584**	0.406	0.413
Bi	**0.475**	-0.416	
As	0.390	**0.670**	-0.272
Sb		**0.661**	
Hg	0.436	-0.170	**0.646**
Au	0.425	0.247	**0.522**
Mo	-0.111		**0.251**

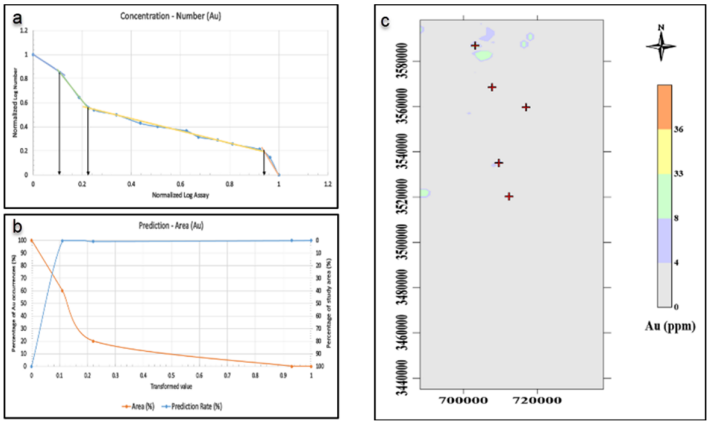

Figure 5. Gold geochemical distribution map, (a) full logarithmic graph of Concentration-Number fractal, (b) Prediction-Area diagram, and (c) fractal-based classification map. The extraction weight is equal to 1.04597

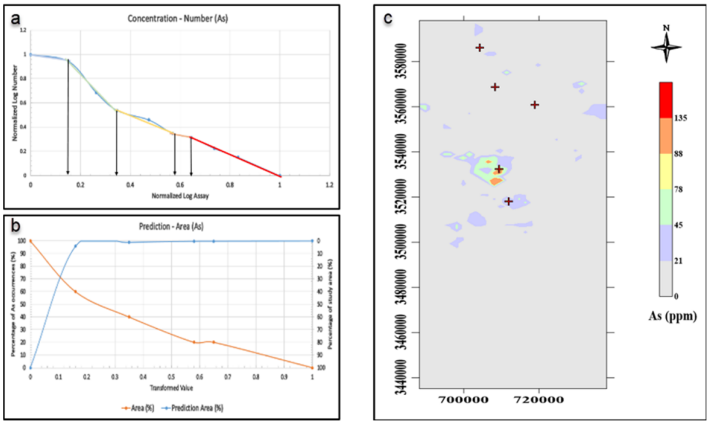

Figure 6. Arsenic geochemical distribution map, (a) full logarithmic graph of Concentration-Number fractal, (b) Prediction-Area diagram, and (c) fractal-based classification map. The extraction weight is equal to 0.94447

For the variable Mercury (Hg) in the logarithmic diagram C-N, five geochemical populations are considered according to the specified trend and the distance between them. We believe the last two populations are anomalous, showing the threshold value of 0.76 in Figure 8-a and in Figure 8-c, shown in orange and red, which can be cited for higher grades 760.0 ppm.

Based on the results in Figure 9-a, we can see four different geochemical populations for the Bismuth (Bi) variable, which has a threshold of 0.55 and considering the last two regions, which are shown in yellow and orange, in Figure 9-C as an abnormal area in the area, it contains grades above 1.21 ppm.

Five geochemical populations for the Molybdenum (Mo) variable are identified in the C-N logarithmic diagram of Figure 10-A. According to studies on the trend and distance of

populations from each other, the last two populations are considered abnormal populations, which show a value of 0.47 on the diagram and are shown in Figure 10-c on a map drawn in orange and red, indicating values above 1.551 ppm.

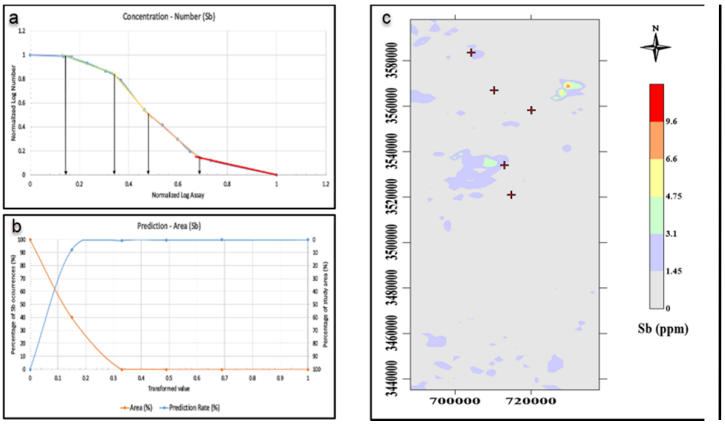

Figure 7. Antimony geochemical distribution map, (a) full logarithmic graph of Concentration-Number fractal, (b) Prediction-Area diagram, and (c) fractal-based classification map. The extraction weight is equal to 0.57536

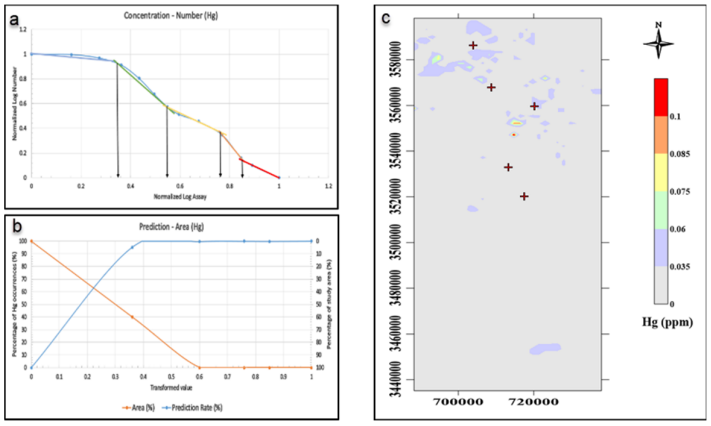

Figure 8. Mercury geochemical distribution map, (a) full logarithmic graph of Concentration-Number fractal, (b) Prediction-Area diagram, and (c) fractal-based classification map. The extraction weight is equal to 0.57536

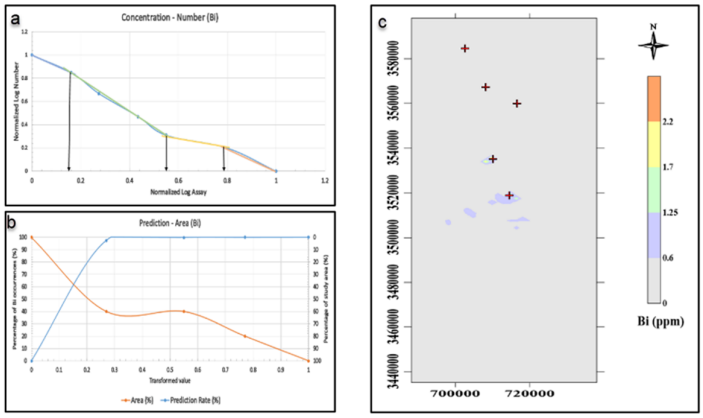

Figure 9. Bismuth geochemical distribution map, (a) full logarithmic graph of Concentration-Number fractal, (b) Prediction-Area diagram, and (c) fractal-based classification map. The extraction weight is equal to 0.48955

As can be seen from the C-N logarithmic diagram for the variable Tin (Sn), according to Figure 11-A, there are five geochemical populations that, given the trend of grade changes and the number of samples available for each, two populations with the threshold value 0.77 for abnormal values, shown in Figure 11-C in orange and red and it contains values above 6.5833 ppm.

Four geochemical populations are considered for the Tungsten variable (W) in the C-N logarithmic diagram. According to the identified trend and the number of mines in the area, which include tungsten with good grades, we consider the last two populations as anomalous populations, which shows the threshold value of 0.76 in Figure 12-a and in Figure 12-c shown in yellow and orange, which can be cited for higher than 177.84 ppm.

Figure 13 shows the classification map of all elements in two classes. The first class is related to the background values, and the second class is connected to the smallest abnormal value in the region. These maps are used to determine the location of mine and mineral occurrences in the study area. In this study, two-class maps are used to check the accuracy of the complete logarithmic fractal diagram of concentration-number and prediction-area diagram for each element.

Prediction-Area curves

The value of the intersection point can be used as a threshold in the P - A diagram of the control layers to create a binary evidence map for use in Boolean MPM logic. Most mineral reserves are related to the intersection area to the maximum.

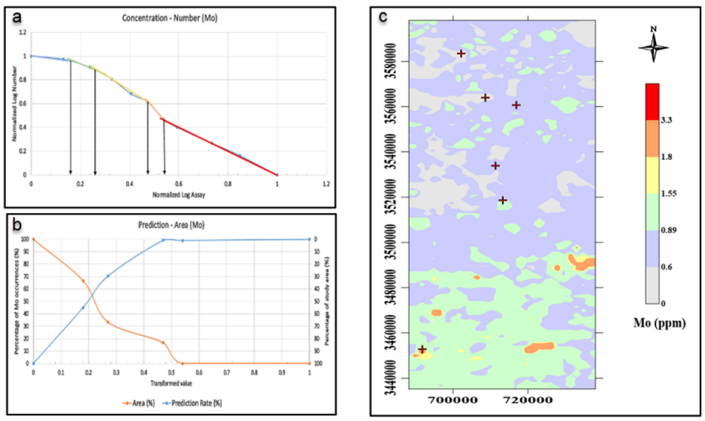

Figure 10. Molybdenum geochemical distribution map, (a) full logarithmic graph of Concentration-Number fractal, (b) Prediction-Area diagram, and (c) fractal-based classification map. The extraction weight is equal to 0.24116

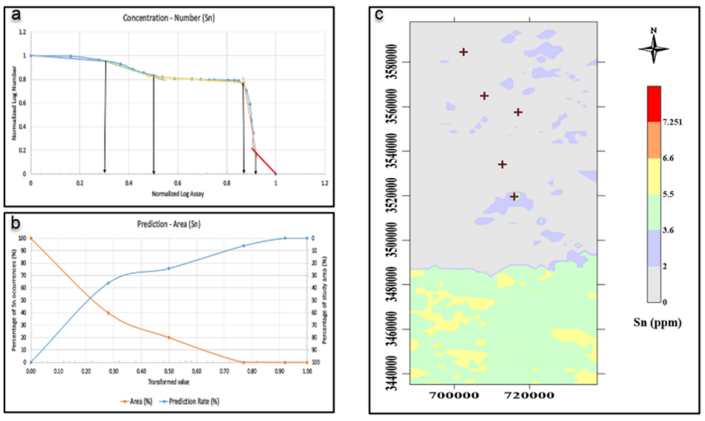

Figure 11. Tin geochemical distribution map, (a) full logarithmic graph of Concentration-Number fractal, (b) Prediction-Area diagram, and (c) fractal-based classification map. The extraction weight is equal to 0.12014

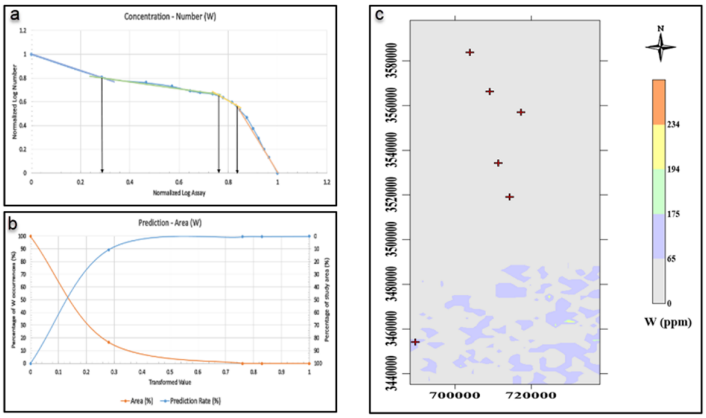

Figure 12. Tungsten geochemical distribution map, (a) full logarithmic graph of Concentration-Number fractal, (b) Prediction-Area diagram, and (c) fractal-based classification map. The extraction weight is equal to 0.08004

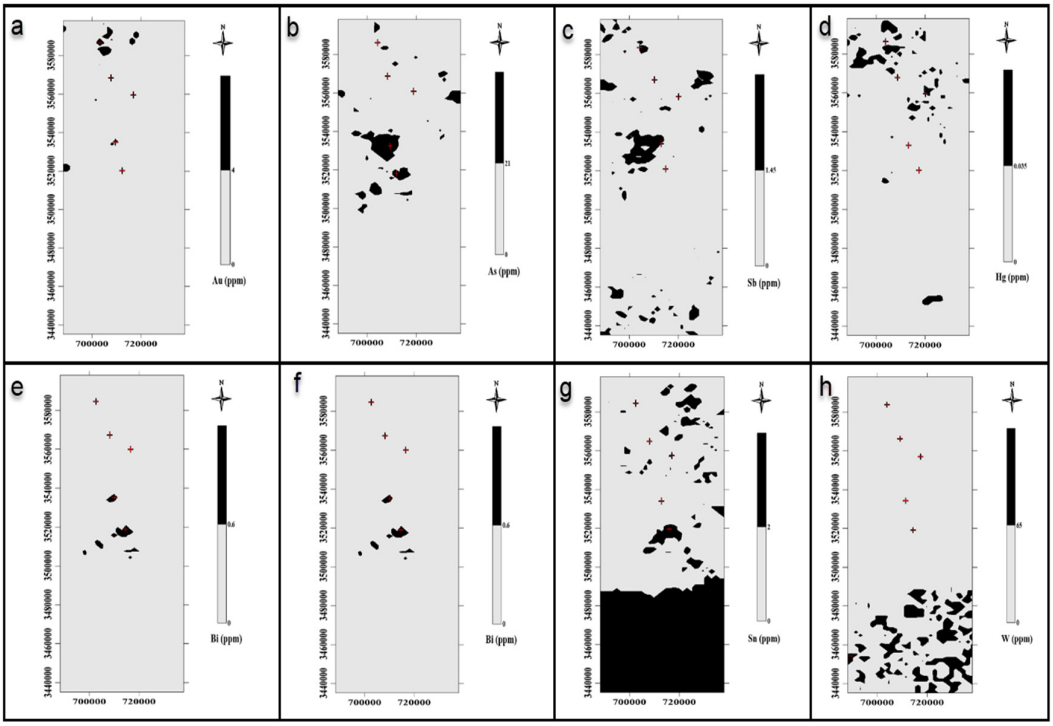

Figure 13. Geochemical distribution map of all elements in two classes, respectively a) Gold, b) Arsenic, c) Antimony, d) Mercury, e) Bismuth, f) Molybdenum, g) Tin and h) Tungsten

In MPM, the weights assigned to spatial evidence should reflect the spatial relationships between the spatial evidence and the intended mineral reserves. Therefore, knowing the Au locations can help the reliability of the weights assigned to the spatial evidence indicating their spatial relationship to mineralization in the Birjand area. There are two curves in a P-A map of a control map: the known mineral occurrence prediction curve and the percentage of occupied areas curve for the classes. Usually, a fractal model is used to separate different populations/classes in a control/evidence map. Since the sum of the prediction rates of the ore occurrence and the space occupied by it at the intersection is 100, if two curves intersect at a location above the P-A diagram of an evidence layer (relative to other control layers), it indicates a smaller area containing more mineral deposits, which means that there is a higher

probability of occurrence of mineral reserves for this class in the indicator/evidence map.

The P-A diagram in Figure 5-b predicts 74% of high mineralization probability in 26% of the studied area. The P-A diagram of the variables shown in Figure 6-b shows 72% of As events in 28% of the study area. In the case of Hg and Sb, it shows 64% of the relevant occurrences in 36% of the area, which is predicted in figure 7-b for antimony and 8-b for mercury, respectively. According to Figure 9-b, in the case of Bi element, 62% of bismuth occurrences have been identified in 38% of the studied area. Figure 10-b predicts 56% of occurrences of Mo element in 44% of the study area. These parameters for Sn and W elements are respectively 53% of mineralization events in 47% of the area for tin, according to Figure 11-b, and for tungsten according to Figure 12-b, 52% of the events are in 48% of the area.

The extracted parameters at the intersections of P-A components for geochemical evidence are given in Table 4.

This study converts the evidence maps' values using a logistic function in the range [0,1]. The weight of individual evidence maps is determined using the P-A diagram by the data-driven method. Eight geochemical maps (W, Sn, Mo, Bi, Hg, Sb, Au, As) were prepared based on the concentration-number fractal method. The geochemical potential integration map by merging all the proven layers is shown in Figure 14-c. The integrated map has five classes (Figure 14-a), the lowest class containing values 0 - 0.18 (light blue) and the highest class containing values 0.78 - 1 (red).

Table 4. Parameters and weights derived from the Prediction-Area curve for Evidence layers.

Elements	Ore Prediction	Occupied Area	Normalize	Weight*
Au	74	26	2.84615	1.04597
As	72	28	2.57143	0.94447
Sb	64	36	1.77778	0.57536
Hg	64	36	1.77778	0.57536
Bi	62	38	1.63158	0.48955
Mo	56	44	1.27273	0.24116
Sn	53	47	1.12766	0.12014
W	52	48	1.08333	0.08004
MPM	88	12	7.33333	1.99243

*Weight is determined through calculating Ln (Ore Prediction/Occupied Area)

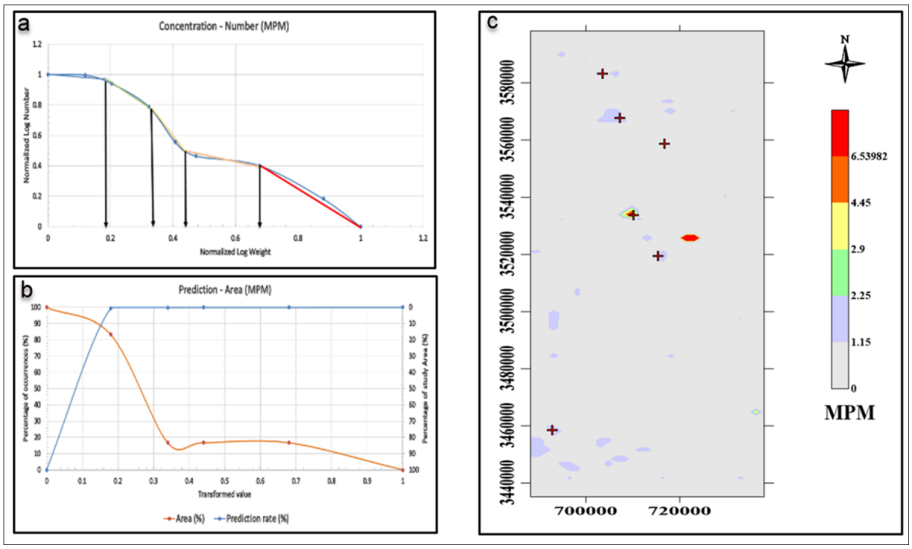

Figure 14. MPM map based on multi overlay index (MOI) method, (a) Full logarithmic fractal diagram of Concentration-Number, (b) Prediction-Area diagram, and (c) Fractal-based classification map. The extraction weight is equal to 1.99243

Based on the intersection point in Figure 14-b, the chemical foresight map occupies 12% of the study area as desirable areas, where 88% of the known Au occurrence is plotted. The composite evidence map weighs more than other geochemical layers (Table 4), which shows its superiority over any other evidence map. The weights are calculated using the natural logarithm of the ore's forecast rate to the occupied area at the intersection. This means that the point of intersection in the MPM's P-A diagram is more valuable (88% > 74, 72, 64, 64, 62, 56, 53, and 52%) than other indicators of multi-class index overlap maps. The final Gold foresight model has the highest ore prediction rate of mineral events among the relevant variables.

Conclusion

In fractal models, highly enriched mineral areas have a strong and significant relationship with the desired locations in the evidence map synthesized in Figure 13-c. The primary anomalous areas As, Au, Bi, Hg, Mo, Sb, Sn and W are in the central parts and have less intensity in the southern and southwestern parts of the region, and similar areas in terms of expansion, are also located in the northern part. The geological map shows that the anomalous areas are mainly Middle to Upper Eocene rocks. In the central part of the study area, anomalies in basalt, andesite, and dacite rocks have been observed, all of which belong to the Eocene period, which shows the most gold anomalies. In the southern and southwestern parts of the study area, anomalies in dacite, andesitic, and basaltic rocks, as well as granodiorite along with diorite and monzonite, are visible. There are signs of gold enrichment in the northern part of the region. The type of host rocks, which are related to the Neogene and pyroclastic types along with apatite and some rocks of the Lower Neogene period, have formed different types of reserves. The correlation between the types of rocks and the elemental distribution of the C-N method shows that andesite, basalt, and dacite are related to gold anomalies in all parts of the study area.
According to the results of integrated evidence layers and maps, some areas can be introduced as new anomalies in the study area, especially in the southwest, south, west and in a smaller scale in north of it.
Another point to note is that a hybrid evidence map with a data-driven multi-class index overlap map can depict desirable areas with higher performance than any evidence. Therefore, this criterion can be placed in an exploratory base as a robust footprint in gold exploration and the need to combine geological and geophysical criteria to reinforce the final synthesis evidence map with higher mine deposit prediction rates and less occupied areas as desirable areas.

Acknowledgment

The authors are grateful to the Geological Survey of Iran “GSI” for data provision.

References

Abedi, M., Fournier, D., Devriese, S.G.R, Oldenburg, D.W., 2018. Potential field signatures along the Zagros collision zone in Iran. Tectonophysics, 722: 25-42.

Afzal, P., Fadakar Alghalandis, Y., Khakzad, A., Moarefvand, P., Rashidnejad Omran, N., 2011. Delineation of mineralization zones in porphyry Cu deposits by fractal concentration–volume modeling. Journal of Geochemical Exploration, 108: 220-232.

Afzal, P., Dadashzadeh Ahari, H., Rashidnejad Omran, N., Aliyari, F., 2013. Delineation of gold mineralized zones using concentration-volume fractal model in Qolqoleh gold deposit, NW Iran. Ore Geology Reviews, 55: 125-133.

Aghanabati, A., 2005. Geology of Iran. Geological Survey of Iran, 586 p.

Almasi, A., Yousefi, M., Carranza, E.J.M., 2017. Prospectivityanalysis of orogenic gold deposits in Saqez-Sardasht Goldfield, Zagros Orogen, Iran. Ore Geology Reviews, 91: 1066–1080.

Arculus, R.J., 1994. Aspects of magma genesis in arcs. Lithos, 33: 189-208.
Bonham-Carter, G. F., Agterberg, F.P., Wright, D.F., 1989. Weights of evidence modelling: A new approach to mapping mineral potential. Statistical Applications in the Earth Sciences, 89: 171–183.
Bissig, T., Clark, A.H., Lee, J.K.W., Quadt, A., 2003. Petrogenetic and metallogenic responses to Miocene slab flattening: new constraints from the EI Indio-Pascua Au–Ag–Cu belt, Chile/Argentina. Mineralium Deposita, 38: 844-862.
Camus, F., Sillitoe, R.H., Petersen, R. (Eds.), 1996. Andean copper deposits: discoveries, mineralization style and metallogeny. Society of Economic Geologists Special Publication, 5: 1-198.
Carranza, E.J.M., Laborte, A.G., 2016. Data-driven predictive modeling of mineral prospectivity using random forests: A case study in Catanduanes Island (Philippines). Natural Resources Research, 25: 35-50.
Cheng, Q., 1999. Spatial and scaling modelling for geochemical anomaly separation. Journal of Geochemical exploration, 65:175-194.
Cheng, Q., Agterberg, F., Bonham-Carter, G., 1996. A spatial analysis method for geochemical anomaly separation. Journal of Geochemical exploration, 56: 183-195.
Cheng, Q., Agterberg, F.P., Ballantyne, S.B., 1994. The separation of geochemical anomalies from background by fractal methods. Journal of Geochemical Exploration, 51: 109-130.
Cooke, D.R., Hollings, P., Walshe, J.L., 2005. Giant porphyry deposits: characteristics, distribution, and tectonic controls. Economic Geology, 100: 801-818.
Corbett, G.J., Leach, T.M., 1998. Southwest Pacific Rim gold–copper systems: structure, alteration and mineralization. Society of Economic Geologists Special Publication, 6: 1-240.
Darabi-Golestan, F., Ghavami-Riabi, R., Khalokakaie, R., Asadi-Haroni, H., Seyedrahimi-Niaraq, M., 2013. Interpretation of lithogeochemical and geophysical data to identify the buried mineralized area in Cu-Au porphyry of Dalli-Northern Hill. Arabian Journal of Geosciences, 6: 4499-4509.
Du, X., Zhou, K., Cui, Y., Wang, J., Zhang, N., Sun, W., 2016. Application of fuzzy Analytical Hierarchy Process (AHP) and Prediction-Area (P-A) plot for mineral prospectivity mapping: A case study from the Dananhu metallogenic belt, Xinjiang, NW China. Arabian Journal of Geosciences, 9: 298.
Gao, Y., Zhang, Z., Xiong, Y., Zuo, R., 2016. Mapping mineral prospectivity for Cu polymetallic mineralization in southwest Fujian Province, China. Ore Geology Reviews, 75: 16-28.
Ghaeminejad, H., Abedi, M., Afzal, P., Zaynali, F., Yousefi, M., 2020. A fractal-based outranking approach for integrating geochemical, geological, and geophysical data. Bollettino Di Geofisica Teorica Ed Applicata, 61 (4): 555-588.
Ghavami-Riabi, R., Seyedrahimi-Niaraq, M., Khalokakaie, R., Hazareh, M., 2010. U-spatial statistic data modeled on a probability diagram for investigation of mineralization phases and exploration of shear zone gold deposits. Journal of Geochemical exploration, 104: 27-33.
Grant, A., 1990. Multivariate statistical analyses of sediment geochemistry. Marine Pollution Bulletin, 21(6): 297-299.
Harris J, Wilkinson L, Grunsky E, Heather K, Ayer, J., 1999. Techniques for analysis and visualization of lithogeochemical data with applications to the Swayze greenstone belt, Ontario. Journal of Geochemical Exploration, 67: 301-334.
Hassanpour, Sh., Afzal, P., 2013. Application of concentration–number (C–N) multifractal modeling for geochemical anomaly separation in Haftcheshmeh porphyry system, NW Iran. Arabian Journal of Geosciences, 6: 957-970.
Hawkes, R.A.W., Webb, H.E., 1979. Geochemistry in mineral exploration, 2nd ed. Academic Press, New York, 657 pp.
Hirst, D.M., 1974. Geochemistry of Sediments from Eleven Black Sea Cores. Geochemistry.
Hou, Z.Q., Zhang, H., Pan, X., Yang, Z., 2011. Porphyry Cu (–Mo–Au) deposits related to melting of thickened mafic lower crust: Examples from the eastern Tethyan metallogenic domain. Ore Geology Reviews, 39: 21-45.
Karar, K., Gupta, A.K., Kumar, A., Biswas, A.K., 2006. Characterization and identification of the sources of chromium, zinc, lead, cadmium, nickel, manganese and iron in PM 10 particulates at the two sites of Kolkata, India. Environmental Monitoring and Assessment, 120(1-3): 347-360.
Kay, S.M., Mpodozis, C., Coira, B., 1999. Neogene magmatism, tectonism, and mineral deposits of the central Andes (22° to 33°S Latitude). B.J. Skinner (Ed.), Geology and Ore Deposits of the Central Andes. Society of Economic Geologist Special Publication, 7: 27-59.

Kerrich, R., Goldfarb, R., Groves, D., Garwin, S., 2000. The characteristics, origins, and geodynamic settings of supergiant gold metallogenic provinces. Science in China, 43: 1-68.

Khalifani, F., Bahroudi, A., Barak, S., Abedi, M., 2019. An integrated Fuzzy AHP-VIKOR method for gold potential mapping in Saqez prospecting zone, Iran. Earth Observation and Geomatics Engineering, 3(1): 21-33.

Li, C.J., Ma, T.H., Shi, J.F., 2003. Application of a fractal method relating concentration and distances for separation of geochemical anomalies from background. Journal of Geochemical Exploration, 77: 167-175.

Malinowski, E.R., Howery, D.G., 1980. Factor analysis in chemistry (p. 10). New York: Wiley.

Mandelbrot, B.B., 1983. The Fractal Geometry of Nature. WH Freeman, San Francisco, 1-468.

Mirzaie, M., Afzal, P., Adib, A., Rahimi, E., & Mohammadi, G. (2020). Detection of zones based on ore and gangue using fractal and multivariate analysis in Chah Gaz iron ore deposit, Central Iran. Journal of Mining and Environment, 11(2): 453-466.

Mitchell, A.H.G., (1973). Metallogenic belts and angle of dip of Benioff zones. Nature, 245: 49-52.

Mohammadpour, M., Bahroudi, A., Abedi, M., Rahimipour, Gh., Jozanikohan, G., Mami Khalifani, F., 2019. Geochemical distribution mapping by combining number-size multifractal model and multiple indicator kriging. Journal of Geochemical Exploration, 200: 13-26.

Nabatian, G., Rastad, E., Neubauer, F., Honarmand, M., Ghaderi, M., 2015. Iron and Fe–Mn mineralisation in Iran: implications for Tethyan metallogeny. Australian Journal of Earth Sciences, 62(2): 211-241.

Nazarpour, A., Omran, N.R., Paydar, G.R., 2015. Application of multifractal models to identify geochemical anomalies in Zarshuran Au deposit, NW Iran. Arabian Journal of Geosciences, 8(2): 877-889.

Nezhad, S.G., Mokhtari, A.R., Rodsari, P.R., 2017. The true sample catchment basin approach in the analysis of stream sediment geochemical data. Ore Geology Reviews, 83: 127-134.

Nykanen, V., Lahti, I., Niiranen, T., Korhonen, K., 2015. Receiver operating characteristics (ROC) as validation tool for prospectivity models-a magmatic Ni–Cu case study from the Central Lapland Greenstone Belt, Northern Finland. Ore Geology Reviews, 71: 853-860.

Panahi, A., Cheng, Q., Bonham-Carter, G.F., 2004. Modelling lake sediment geochemical distribution using principal component, indicator kriging and multifractal power-spectrum analysis: a case study from Gowganda, Ontario. Geochemistry: Exploration, Environment, Analysis, 4(1): 59-70.

Peacock, S.M., 1993. Large-scale hydration of the lithosphere above subducting slabs. Chemical Geology, 108: 49-59.

Perello, J., Carlotto, V., Zarate, A., Ramos, P., Posso, H., Neyra, C., Caballero, A., Fuster, N., Muhr, R., 2003. Porphyry-style alteration and mineralization of the Middle Eocene to early Oligocene Andahualas–Yauri belt, Cuzco region, Peru. Economic Geology, 98: 1575-1606.

Qiuming, C., 2000. Multifractal theory and geochemical element distribution pattern, Earth Science. Journal of China University of Geosciences, 25: 311-318.

Richards, J.P., Boyce, A.J., Pringle, M.S., 2001. Geologic evolution of the Escondida area, northern Chile: a model for spatial and temporal location of porphyry Cu mineralization. Economic Geology, 96: 271-306.

Richards, J., Wilkinson, D., Ullrich, T., 2006. Geology of the Sari Gunay epithermal gold deposit, Northwest Iran. Econ. Geol. 101: 1455-1496.

Riemann, C., Filzmoser, P., Garrett, R.G., 2002. Factor analysis applied to regional geochemical data: problems and possibilities. Applied geochemistry, 17(3): 185-206.

Roshanravan, B., Aghajani, H., Yousefi, M., Kreuzer, O., 2019. An improved prediction-area plot for prospectivity analysis of mineral deposits. Natural Resources Research, 28(3): 1089-1105.

Seydi, A., Abedi, M., Bahroudi, A., Ferdowsi, H., 2023. Geochemical prospectivity of Cu-mineralization through Concentration-Number fractal modeling and Prediction-Area plot: a case study in east Iran. International Journal of Mining and Geo-Engineering, 57(2): 159-169.

Seyedrahimi-Niaraq, M., Hekmatnejad, A., 2020. The efficiency and accuracy of probability diagram, spatial statistic and fractal methods in the identification of shear zone gold mineralization: a case study of the Saqqez gold ore district, NW Iran. Acta Geochimica, 40: 78-88.

Sillitoe, R.H., 2003. Iron oxide-copper-gold deposits: an Andean view. Mineralium Deposita, 38: 787-812.

Sillitoe, R.H., 1993. Gold-rich porphyry copper deposits: geological model and exploration implication. Mineral Deposit Modeling. Geological Association of Canada Special Paper, 40: 465-478.

Sillitoe, R.H., 1972. A plate tectonic model for the origin of porphyry copper deposits. Economic Geology, 67: 184-197.

Skewes, M.A., Stern, C.R., 1995. Genesis of the giant late Miocene to Pliocene copper deposits of central Chile in the context of Andean magmatic and tectonic evolution. International Geology Review, 37(10): 893-909.

Sprovieri, R., Thunell, R., Howe, M., 2020. Paleontological and geochemical analysis of three laminated sedimentary units of late Pliocene-early Pleistocene age from the Monte San Nicola section in Sicily. Rivista Italiana di Paleontologia e Stratigrafia, 92(3).

Tahernejad, M.M., Khalo Kakaei, R., Ataei, M., 2018. Analyzing the effect of ore grade uncertainty in open pit mine planning; A case study of Rezvan iron mine, Iran. International Journal of Mining and Geo-Engineering, 52(1): 53-60.

Wu, R., Chen, J., Zhao, J., Chen, J., Chen, S., 2020. Identifying Geochemical Anomalies Associated with Gold Mineralization Using Factor Analysis and Spectrum–Area Multifractal Model in Laowan District, Qinling-Dabie Metallogenic Belt, Central China. Minerals, 10(3): 229.

Yousefi, M., Carranza, E.J.M., 2015. Prediction–area (P-A) plot and C–A fractal analysis to classify and evaluate evidential maps for mineral prospectivity modeling. Computers & Geosciences, 79: 69-81.

Yousefi, M., Carranza, E.J.M., 2016. Data-driven index overlay and Boolean logic mineral prospectivity modeling in greenfields exploration. Natural Resources Research, 25: 3-18.

Zhang, N., Zhou, K., Du, X., 2017. Application of fuzzy logic and fuzzy AHP to mineral prospectivity mapping of porphyry and hydrothermal vein copper deposits in the Dananhu-Tousuquan island arc, Xinjiang, NW China. Journal of African Earth Sciences, 128: 84-96.

Zuo, R., 2011. Decomposing of mixed pattern of arsenic using fractal model in Gangdese belt, Tibet. China. Appl. Geochem. 26: S271-S273.

Zumlot, A.B.T., 2012. Multivariate statistical approach to geochemical methods in water quality factor identification; application to the shallow aquifer system of the Yarmouk Basin of north Jordan. Research Journal of Environmental and Earth Sciences, 4(7): 756-768.

Zuo, R., Wang, J., 2016. Fractal/multifractal modeling of geochemical data: a review. Journal of Geochemical Exploration, 164: 33-41.